Effect of solid-solution strengthening on deformation mechanisms and strain hardening in medium-entropy $V_{1-x}Cr_xCoNi$ alloys

Chung, Hyun; Kim, Dae Woong; Cho, Woo Jin; Han, Heung Nam; Ikeda, Yuji; Ishibashi, Shoji; Körmann, Fritz; Sohn, Seok Su

DOI
10.1016/j.jmst.2021.07.042

Publication date
2022

Document Version
Final published version

Published in
Journal of Materials Science and Technology

Journal of Materials Science & Technology 108 (2022) 270–280

Contents lists available at ScienceDirect

Journal of Materials Science & Technology

journal homepage: www.elsevier.com/locate/jmst

Research Article

Effect of solid-solution strengthening on deformation mechanisms and strain hardening in medium-entropy $V_{1-x}Cr_xCoNi$ alloys

Hyun Chung[a], Dae Woong Kim[b], Woo Jin Cho[c], Heung Nam Han[c], Yuji Ikeda[d,e], Shoji Ishibashi[e,f], Fritz Körmann[e,g], Seok Su Sohn[a,*]

[a] Department of Materials Science and Engineering, Korea University, Seoul 02841, South Korea
[b] Center for High Entropy Alloys, Pohang University of Science and Technology, Pohang 37673, South Korea
[c] Department of Materials Science and Engineering and Research Institute of Advanced Materials, Seoul National University, Seoul 08826, South Korea
[d] Institute for Materials Science, University of Stuttgart, Pfaffenwaldring 55, Stuttgart 70569, Germany
[e] Computational Materials Design, Max–Planck–Institut für Eisenforschung GmbH, Max–Planck–Strabe 1, Düsseldorf 40237, Germany
[f] Research Center for Computational Design of Advanced Functional Materials (CD-Fmat), National Institute of Advanced Industrial Science and Technology (AIST), Tsukuba, Ibaraki 305-8568, Japan
[g] Department of Materials Science and Engineering, Delft University of Technology, Mekelweg, 2, Delft 2628 CD, the Netherlands

ARTICLE INFO

Article history:
Received 8 June 2021
Revised 12 July 2021
Accepted 16 July 2021
Available online 30 October 2021

Keywords:
Medium-entropy alloy
Tensile property
Solid-solution strength
Strain-hardening rate
Stacking fault energy

ABSTRACT

High- and medium-entropy alloys (HEAs and MEAs) possess high solid-solution strength. Numerous investigations have been conducted on its impact on yield strength, however, there are limited reports regarding the relation between solid-solution strengthening and strain-hardening rate. In addition, no attempt has been made to account for the dislocation-mediated plasticity; most works focused on twinning- or transformation-induced plasticity (TWIP or TRIP). In this work we reveal the role of solid-solution strengthening on the strain-hardening rate via systematically investigating evolutions of deformation structures by controlling the Cr/V ratio in prototypical $V_{1-x}Cr_xCoNi$ alloys. Comparing the TWIP of CrCoNi with the dislocation slip of $V_{0.4}Cr_{0.6}CoNi$, the hardening rate of CrCoNi was superior to slip-band refinements of $V_{0.4}Cr_{0.6}CoNi$ due to the dynamic Hall-Petch effect. However, as *V* content increased further to $V_{0.7}Cr_{0.3}CoNi$ and VCoNi, their rate of slip-band refinement in $V_{0.7}Cr_{0.3}CoNi$ and VCoNi with high solid-solution strength surpassed that of CrCoNi. Although it is generally accepted in conventional alloys that deformation twinning results in a higher strain-hardening rate than dislocation-mediated plasticity, we observed that the latter can be predominant in the former under an activated huge solid-solution strengthening effect. The high solid-solution strength lowered the cross-slip activation and consequently retarded the dislocation rearrangement rate, i.e., the dynamic recovery. This delay in the hardening rate decrease, therefore, increased the strain-hardening rate, results in an overall higher strain-hardening rate of *V*-rich alloys.

1. Introduction

Multicomponent high- or medium-entropy alloys (HEAs or MEAs) have been spotlighted owing to their extraordinary mechanical properties such as high solid-solution strengthening, enhanced strength and ductility at cryogenic temperature, and high fracture toughness [1–3]. HEAs and MEAs with over three elements and near-equiatomic compositions enable the formation of a single-phase solid solution in the absence of intermetallic compounds, unlike conventional dilute solid solutions. The CrCoNi alloy is one of the most prominent single-phase fcc (face-centered cubic) -structured MEA of the CrMnFeCoNi alloy family, exhibiting excellent tensile properties and fracture toughness attributed from deformation-induced twinning and phase transformation by low stacking fault energy (SFE) and high solid-solution strengthening effect [4–7]. Recently, Sohn et al. [8] reported an fcc-structured VCoNi alloy performing outstanding yield strength of approximately 1 GPa. This high yield strength mainly results from the high solid-solution strengthening and grain boundary strengthening. In addition, the alloy exhibits adequate ductility and strain hardening owing to the formation of nanosized dislocation substructure without secondary strengthening mechanisms, such as twinning and martensitic transformation even at cryogenic temperature [9].

In addition to the aforementioned properties, previous studies presented several detailed perspectives regarding the origin of solid-solution strengthening in HEAs and MEAs: solute misfit volumes increasing the interaction energies between the local spa-

* Corresponding author.
E-mail address: sssohn@korea.ac.kr (S.S. Sohn).

https://doi.org/10.1016/j.jmst.2021.07.042
1005-0302/

tial fluctuations in solute concentrations and the dislocations [10]; charge transfer or atomic-level pressure, originating from atomic size, electronic state [11]; and short-range order (SRO) or cluster (SRC), enabling additional elemental interaction to act as barriers when dislocation glides [12]. It is clear that the solid-solution strengthening, or often referred to a friction stress, increases in the following order: CrMnFeCoNi < CrCoNi < VCoNi alloys; however, its origin has not been properly elucidated. Nevertheless, *V* has recently been perceived as an optimal alloying element because of the large atomic volume misfit, which enhances the yield strength in both fcc and bcc HEAs [10]. For example, the different observed impact on the yield strength of CrCoNi and VCoNi alloys suggest that the tensile properties can be tailored by controlling the fractions of Cr and *V* in the $V_{1-x}Cr_xCoNi$ system.

Moving on to the plasticity regime in stress-strain curves, the deformation behavior directly affects the strain hardening capability and determines the tensile strength and ductility. As mentioned above, the CrCoNi alloy shows deformation-induced twinning, while the VCoNi alloy only exhibits dislocation glides with planar slip, leading to slip-band refinement [4,5,8]. This can be related to the SFEs, i.e., the observed deformation mechanisms suggest a low SFE for CrCoNi and a high SFE for VCoNi, respectively. Whereas the SFE for CrCoNi is estimated to be -42 mJ m^{-2} and 22 mJ m^{-2} via calculations and experiments, respectively, these approaches have not yet been reported for VCoNi [8,13–15]. In addition, SFE is not an absolute parameter that determines the deformation mechanism. The existence of short-range order (SRO) and solid-solution strengthening effects also stronlgy influence the planar slip behavior. Hughes [16] investigated Al-Mg alloys and reported that increased friction stress, i.e., the solid-solution strength, by the solute Mg atoms primarily causes a transition from cell structure to Taylor lattice. Similarly, the effects of SRO on Ag, Cu, and Ni alloys have been investigated, where the destruction of SRO by leading dislocations causes glide plane softening and consequent planar slip behavior [17]. Therefore, further investigation is required in terms of hardening to reveal the underlying mechanisms regarding factors with predominant effect on slip planarity and resulting strain-hardening rate.

Therefore, although numerous studies have thoroughly investigated the solid-solution strengthening effect on the yield strength, there are limited reports regarding the relationship between the solid-solution strengthening and the strain-hardening rate in HEAs and MEAs. In addition, the effect of deformation mechanisms on the associated strain-hardening rate mostly considers deformation-twinning or deformation-induced martensitic transformation in HEAs and MEAs; no attempt has been made to account for the dislocation-mediated plasticity. To reveal the role of solid-solution strengthening on the strain-hardening rate, we chose two representative model alloys: CrCoNi and VCoNi. Accordingly, the fractions of Cr and V were tailored to systematically investigate the evolution of deformation structures and their contributions to the strain-hardening rate. Although it is generally accepted that deformation twinning leads to a higher strain-hardening rate than dislocation-mediated plasticity owing to the so-called dynamic Hall-Petch effect, we found that the latter can be predominant to the former under activated huge solid-solution strengthening effect. Its origin was discussed in terms of the elemental effect, solid-solution strengthening, SFE, and transitions of deformation mechanisms.

2. Experimental and computational details

2.1. Fabrication

Ingots of $V_{1-x}Cr_xCoNi$ (x = 0, 0.3, 0.6, 1) alloys were fabricated by vacuum induction melting (MC100V, Indutherm, Walzbachtal-Wössingen, Germany) using high-purity pure elements (>99.95 wt%), zirconia crucible, and graphite mold (100 × 35 × 8 mm^3). The ingots were homogenized at 1200 °C for 24 h in an Ar-atmosphere furnace, followed by water quenching. The surface scale was first removed by pickling in a 20% HCl solution for 20 s. Then, the ingots were cold-rolled with ~80% thickness reduction. The cold-rolled sheets (thickness: 1.5 mm) were annealed at 900–1200 °C for 10–60 min under Ar atmosphere to obtain various grain sizes for each alloy, followed by water-quenching to room temperature.

2.2. Microstructural characterization

Phase identification and grain size measurements were conducted by electron backscatter diffraction (EBSD) using a field-emission scanning electron microscope (FE-SEM, JSM-6500F, JEOL, USA). The deformation structure was analyzed by EBSD and electron channeling contrast imaging (ECCI) analyzed using a Zeiss-Merlin instrument (ZEISS Crossbeam 1540 EsB, ZEISS, Oberkochen, Germany). The end-specimen quality was subjected to mechanical polishing using a colloidal silica suspension for 0.5 h.

2.3. Mechanical tests and modulus measurement

Flat dog-bone specimens were prepared with gage length, gage width, and thickness of 6.4, 2.5, and 1.5 mm, respectively. Tensile specimens were cut from the annealed sheets by electrical discharge machining. Uniaxial tensile tests were carried out using a universal testing machine (Instron 8801, Canton, MA, USA) at an initial strain rate of 6.4 × 10^{-3} mm s^{-1}. Tensile strains were measured using a digital image correlation (DIC) method (ARAMIS 5 M, GOM mbH, Germany). The tensile tests were repeated at least three times to ensure reliability.

The shear modulus (G) and Young's modulus (E) for $V_{0.7}Cr_{0.3}CoNi$ and $V_{0.4}Cr_{0.6}CoNi$ alloys were measured using an ultrasonic pulse-echo measuring system (HKL-01-UEMT, HKLAB CO., Korea) at room temperature. A specimen of 20 × 20 × 1.5 mm^3 was polished mechanically and then tested five times. Poisson's ratio (ν) was calculated using an elastic equation for isotropic bodies [18].

2.4. Ab initio calculations

Ab initio calculations were conducted for four $V_{1-x}Cr_xCoNi$ alloys with x = 0, 1/3, 2/3, and 1. To compute the SFEs, both the fcc and the hexagonal close-packed (hcp) phases were considered. The c/a ratio of the hcp phase is fixed to the ideal value of $(8/3)^{1/2} \approx 1.633$. To improve the computational accuracy, both structures were modeled by 54-atom supercells with identical supercell shapes consisting of six close-packed layers in each simulation cell and nine atoms in each layer. Chemical disorder was simulated by special quasi-random structures (SQS) [19], with minimization of the correlation functions of the first several nearest-neighbor pairs. To achieve better statistics, we considered several inequivalent SQS models for each composition, depending on computed properties as discussed below. Mean-squared atomic displacements (MSADs) were derived from the relaxed atomic positions. The atomic relaxations as well as the corresponding total energies to calculate the SFEs were computed using the VASP code [20–22] within the framework of the density functional theory (DFT) and the projector-augmented wave (PAW) method [23]. The exchange-correlation energy has been treated within the generalized gradient approximation (GGA) of the Perdew–Burke–Ernzerhof (PBE) form [24]. A plane wave cut-off energy of 300 eV was chosen for all calculations. The 3d 4 s orbitals of V, Cr, Co, and Ni were treated as valence states. The Brillouin zones were sampled

Table 1
Difference in atomic radii (δ_r), average valence electron concentration (VEC), mixing enthalpy (ΔH_{mix}), electronegativity difference ($\Delta\chi$), elastic modulus (E), shear modulus (G), and Poisson's ratio (ν) of the $V_{1-x}Cr_xCoNi$ (x = 0, 0.3, 0.6, 1) alloys.

Specimen	δ_r(%)	VEC	ΔH_{mix}(kJ mol^{-1})	$\Delta\chi$	E(GPa)	G(GPa)	ν
VCoNi [8]	6.2	8	- 14.2	0.156	192	72	0.334
$V_{0.7}Cr_{0.3}$CoNi	5.8	8.1	- 11.6	0.143	235	90	0.308
$V_{0.4}Cr_{0.6}$CoNi	5.4	8.2	- 8.8	0.127	223	85	0.313
CrCoNi [8]	4.8	8.3	- 4.9	0.1	211	87	0.286

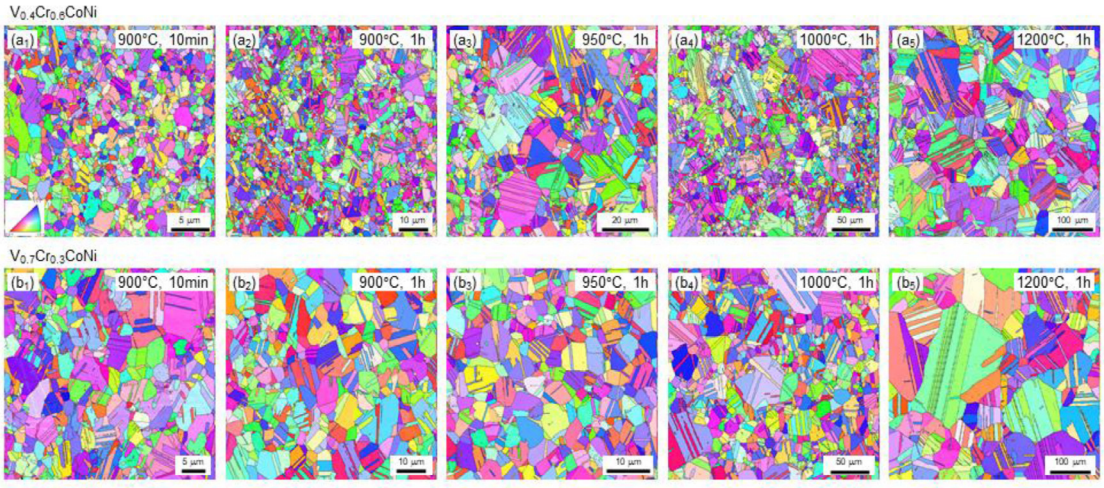

Fig. 1. EBSD IPF maps of the annealed $V_{0.4}Cr_{0.6}$CoNi and $V_{0.7}Cr_{0.3}$CoNi alloys at (a_1, b_1) 900 °C for 10 min, (a_2, b_2) 900 °C for 1 h, (a_3, b_3) 950 °C for 1 h, (a_4, b_4) 1000 °C for 1 h, and (a_5, b_5) 1200 °C for 1 h.

by a Γ-centered 6 × 6 × 4 k-point mesh for the 54-atom super-cell models and by the Methfessel and Paxton scheme [25] with a smearing width of 0.1 eV. The total energies were minimized until they converged within 1 × 10^{-3} eV per simulation cell. The internal atomic coordinates were optimized until all the forces on the atoms converged within 5 × 10^{-2} eV/Å, while the cell shapes were fixed. All the calculations were performed considering spin polarization. Ten inequivalent SQS models were considered for each composition. The fcc lattice parameter of 3.6 Å, which close to the epxerimental values of the investigated alloys, was mainly focused on, and six volumes around the experiental value were computed for each SQS configuration. The lattice vibrational contributions to the Helmholtz energies were then evaluated based on the Debye–Grüneisen model [26], where the Debye temperatures were computed based on the bulk moduli obtained from the energy–volume functions fitted to the Vinet equation of state [27,28]. The SFEs of $V_{1-x}Cr_xCoNi$ in the fcc phase at the given volume were computed based on the first-order axial Ising model (AIM1) [29] as:

$$SFE \approx \frac{2\left(F^{hcp} - F^{fcc}\right)}{A} \quad (1)$$

where F^{α} denotes the Helmholtz energy of the phase α (fcc or hcp), and A denotes the total area of the close-packed layers.

To calculate the Bader volumes (V_{Bader}) and the Bader charges (ρ_{Bader}) [30], as well as the atomic-level pressures (σ_{Bader}) evaluated in the Bader volumes, the QMAS code [31] within the framework of DFT and the PAW method [23] was employed. The exchange-correlation energy was treated within the GGA of the PBE form [24]. The plane-wave cut-off energy was set to 20 Ha (544 eV). The Brillouin zones were sampled by a Γ-centered 6 × 6 × 4 k-point mesh for the 54-atom super-cell models and by the Gaussian-smearing scheme [32] with the full width at half maximum (FWHM) of 25 meV. The total energies were minimized until for each ionic step the charge differences became less than 1 × 10^{-8} per simulation cell, and internal atomic positions were relaxed until the residual forces became less than 5 × 10^{-5} Ha/bohr (2.5 × 10^{-3} eV/Å). All the calculations were performed considering spin polarization. Five inequivalent SQS models were considered for each composition. The internal atomic positions were re-optimized from the VASP-optimized ones. Note that the more accurate convergence parameters were required for the computation of atomic-level stresses as compared to the more robust total energies and MSAD values.

To compute atomic stresses, we utilized the electronic-structure-based stress densities introduced by Filippetti and Fiorentini [33] and later modified to fit the plane-wave basis PAW method [34]. The atomic-level pressure was computed as the diagonal average of the atomic stress. In the present study, positive and negative values indicate compressive and tensile stresses, respectively.

3. Results

3.1. Microstructure

The relative phase stability between solid-solution phases and intermetallic compounds is determined according to the thermodynamic parameters and estimated by empirical formation rules based on the Hume-Rothery rules [35,36]. The empirical bounds to form a single fcc solid-solution phase are the difference in atomic radii ($\delta_r \leq 6.6\%$), average valence electron concentration (VEC ≥ 8), and mixing enthalpy (−15 kJ mol^{-1} < ΔH_{mix} < 5 kJ mol^{-1}). For the present alloys, the corresponding values are well satisfied with the empirical conditions to form fcc phase, as listed in Table 1.

Fig. 1(a_1–b_5) shows EBSD inverse pole figure (IPF) maps for fully recrystallized $V_{1-x}Cr_xCoNi$ (x = 0.3, 0.6) alloys with varying isothermal heat-treatment conditions between 900 and 1200 °C for 10–60 min. The average grain size was measured by considering

Table 2
Room temperature tensile properties and average grain sizes of the $V_{1-x}Cr_xCoNi$ (x = 0, 0.3, 0.6, 1) alloys according to various annealing conditions.

Specimen	Annealing Condition	Average Grain Size(μm)	YS (MPa)	UTS(MPa)	El.(%)
VCoNi [8]	900 °C, 10 min	2.0 ± 1.5	991 ± 8	1359 ± 2	38 ± 0.5
	900 °C, 1 h	5.6 ± 3.1	767 ± 5	1221 ± 1	46 ± 0.1
	950 °C, 1 h	18.7 ± 13.9	602 ± 7	1123 ± 8	51 ± 1.6
	1000 °C, 1 h	27.8 ± 19.5	517 ± 8	1049 ± 1	55 ± 1.5
	1200 °C, 1 h	122.2 ± 76.4	461 ± 6	886 ± 4	58 ± 0.1
$V_{0.7}Cr_{0.3}CoNi$	900 °C, 10 min	3.6 ± 2.8	956 ± 11	1232 ± 5	40.1 ± 1.2
	900 °C, 1 h	5.0 ± 2.5	852 ± 8	1183 ± 3	42.9 ± 1.4
	950 °C, 1 h	6.4 ± 3.2	657 ± 7	1087 ± 4	49.2 ± 0.8
	1000 °C, 1 h	14.4 ± 9.2	587 ± 5	1051 ± 6	52.5 ± 1.4
	1200 °C, 1 h	54.6 ± 33.1	449 ± 7	927 ± 7	64.9 ± 2.2
$V_{0.4}Cr_{0.6}CoNi$	900 °C, 10 min	2.1 ± 1.4	737 ± 8	1061 ± 5	47.9 ± 1.5
	900 °C, 1 h	2.4 ± 1.5	598 ± 7	991 ± 10	54.5 ± 2.4
	950 °C, 1 h	5.3 ± 3.3	537 ± 7	951 ± 11	56.5 ± 3.3
	1000 °C, 1 h	10.1 ± 7.8	472 ± 9	920 ± 5	61.5 ± 1.8
	1200 °C, 1 h	31.4 ± 16.7	404 ± 7	842 ± 2	68.2 ± 2.2
CrCoNi [8]	900 °C, 1 h	11.0 ± 6.7	389 ± 6	883 ± 5	68 ± 1.2

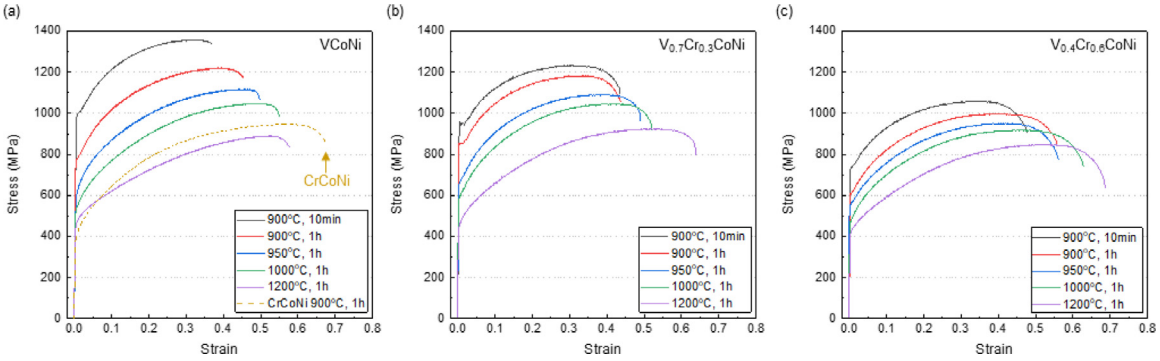

Fig. 2. Engineering stress–strain curves at room-temperature for the fully recrystallized $V_{1-x}Cr_xCoNi$ (x = 0, 0.3, 0.6, 1) alloys under different heat treatments: (a) VCoNi and CrCoNi [8], (b) $V_{0.7}Cr_{0.3}CoNi$, (c) $V_{0.4}Cr_{0.6}CoNi$ alloys.

twin boundaries as normal random boundaries. Table 2 summarizes the grain size for all $V_{1-x}Cr_xCoNi$ (x = 0, 0.3, 0.6, 1) specimens in which the sizes for the VCoNi and CrCoNi alloys are quoted from the literature [8]. The grain size of VCoNi increases from 2.0 to 122.2 μm under the mentioned heat-treatment conditions. As the Cr content increases from 10 at.% ($V_{0.7}Cr_{0.3}CoNi$) to 20 at.% ($V_{0.4}Cr_{0.6}CoNi$), the grain size increases from 3.6 μm to 54.6 μm and from 2.1 μm to 31.4 μm, respectively, for identical annealing conditions.

3.2. Solid-solution strengthening and Hall-Petch relationship

The engineering stress-strain curves for the $V_{1-x}Cr_xCoNi$ (x = 0, 0.3, 0.6, 1) alloys with different grain sizes are shown in Fig. 2(a–c). For each alloy having similar average grain size, i.e., CrCoNi of 11.0 μm, $V_{0.4}Cr_{0.6}CoNi$ of 10.1€μm, $V_{0.7}Cr_{0.3}CoNi$ of 6.4€μm, and VCoNi of 5.6 μm, increasing V content leads to the enhancement in yield strength from 389 to 767 MPa, the tensile strength from 883 to 1221 MPa, while the ductility reduces from 68 to 46%. The highest yield strength of VCoNi alloy could be attributed to the relatively smaller grain size, though for VCoNi with grain size of 18.7 μm, the yield strength is 602 MPa, which is still larger as compared to other alloys having smaller grain size. The detailed tensile properties for the $V_{1-x}Cr_xCoNi$ (x = 0, 0.3, 0.6, 1) alloys are listed in Table 2.

The yield strength increases as the grain size decreases according to the well-known Hall-Petch relationship. From the measured grain sizes (D), the solid-solution strength (σ_0) and Hall-Petch coefficient (k_y) in Eq. (2) were quantified for each $V_{1-x}Cr_xCoNi$ (x = 0, 0.3, 0.6, 1) alloy.

$$\sigma_y = \sigma_0 + k_y D^{-1/2} \quad (2)$$

From CrCoNi to VCoNi, σ_0 increases from 216 to 383 MPa and k_y increases from 568 to 864 MPa $\mu m^{1/2}$ with increasing V content.

In conventional dilute solid solutions, the strain energy produced by the atomic size difference hinders the dislocation glide, leading to a solid-solution strengthening effect. However, HEAs and MEAs require further consideration where the environment around the elements is immensely divergent from the locally different and random constituent atoms than the traditional alloys. The atomic-level pressure has been reported to determine the strengthening effect considering the misfit of elements with respect to atomic size, electronic state, and charge transfer [11]. Based on weak-pinning Labusch model [37], plotting atomic-level pressure with experimental values of solid-solution strength from binary to quinary alloys, atomic-level pressure appears reliable in predicting solid-solution strengthening. For simplicity in calculation, Oh et al. [11] reported that the computationally more expensive atomic-level pressure calculations can be also replaced with an electronegativity difference. The calculated difference in atomic size misfit and electronegativity in Table 1 indicates a linear relationship with the experimentally measured solid-solution strength.

To further investigate the relationship between solid-solution strengthening and atomistic properties, the MSADs, as well as the standard deviations (SDs) of Bader charge (charge transfer) and atomic-level pressure were computed based on *ab initio* calculations. The MSAD quantifies the local lattice distortion [38], while the distribution of the atomic charges shows how the elements

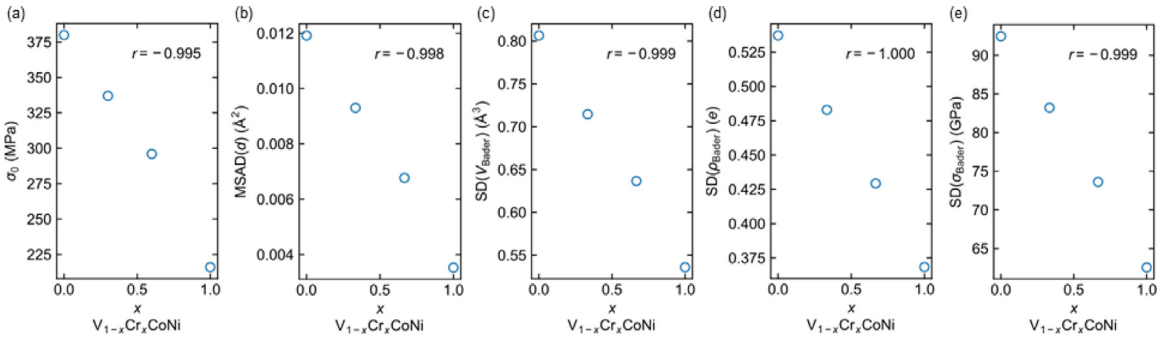

Fig. 3. (a) Experimental solid-solution strengths (σ_0), (b) *ab initio* computed MSADs, (c) Bader volumes (V_{Bader}), (d) Bader charges (ρ_{Bader}), and (e) atomic-level pressures (σ_{Bader}) as functions of the Cr content. The Pearson correlation coefficients r are also shown in the panels.

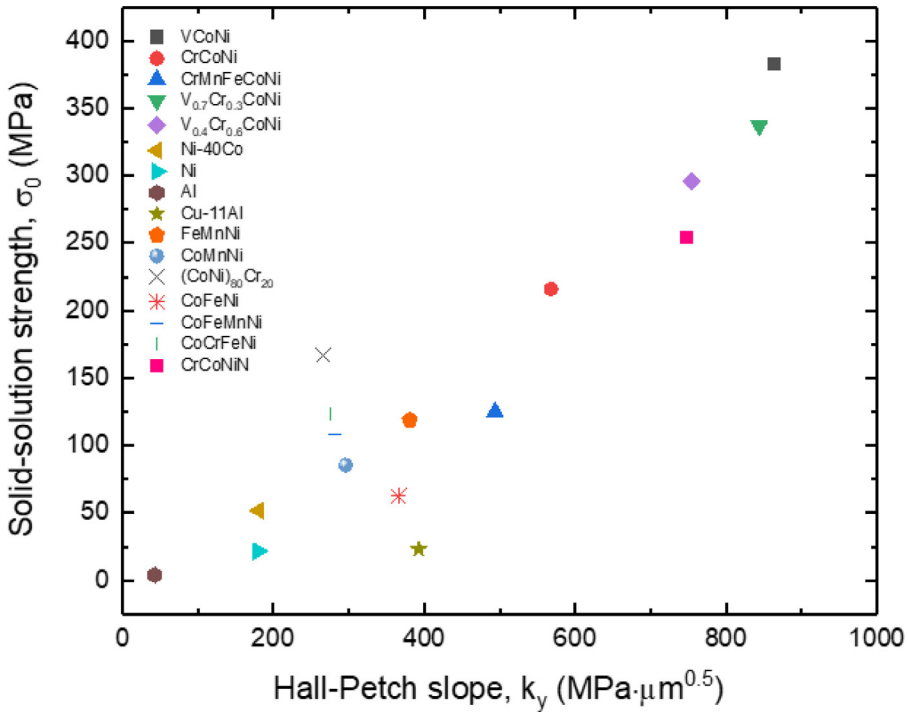

Fig. 4. Plotted solid-solution strength with Hall-Petch coefficients of the VCrCoNi alloys, compared with other HEAs and MEAs, binary alloys, and pure metals.

affect one another electronically [11]. Fig. 3(a) shows the solid-solution strengths (σ_0) in experiments as a function of the Cr content. A very strong correlation between σ_0 and the Cr content is found, where σ_0 increases with V content. Fig. 3(b) shows *ab initio* computed MSADs as functions of the Cr content. Similar to the experimental σ_0, the MSADs also show a strong correlation with Cr content. This also implies a correlation between computed MSADs and experimental σ_0 which is consistent with previous studies of the relationship between MSAD and lattice friction stress [8,38]. Fig 3(c–e) shows the SD of Bader volumes, Bader charges, and atomic-level pressure as functions of the Cr content (see the Appendix for further detail). Similar to the experimental σ_0 and the *ab initio* MSADs, these Bader-analysis-based values show also a clear correlation with the Cr content. This supports the previously reported correlation in HEAs/MEAs between solid-solution strength and atomic charge transfer or atomic-level pressure [11].

In addition to the solid-solution strength, grain boundary strengthening is another primary factor contributing to the yield strength of fully recrystallized single fcc-structured MEAs. Fig. 4 plots σ_0 with k_y values for the present alloys and the values from previous reports [12,39–41]. Evidently, the overall relationship between σ_0 and k_y is almost linearly proportional from pure metals to HEAs and MEAs. This indicates that an increase in the solid-solution strength has a strong tendency with an increase in grain size sensitivity to strengthening. A previous study reported that, according to interior source model describing a dislocation generation by Frank-Read source in lattices, friction stress also affects the Hall-Petch coefficient [8]. The high Peierls stress induced by lattice distortion with relatively short dislocation width leads to high k_y value via high critical resolve shear stress (CRSS). The $V_{1-x}Cr_xCoNi$ (x = 0, 0.3, 0.6, 1) alloys in this study fits well into the results in the previous report.

3.3. Strain hardening

The effect of grain size on the comparison of strain-hardening rate for each alloy was reduced by considering specimens with similar grain sizes as aforementioned. Fig. 5(a) shows true stress-strain curves for the selected alloys and Fig. 5(b) displays the strain-hardening rate ($\theta = d\sigma/d\varepsilon$) of the $V_{1-x}Cr_xCoNi$ (x = 0, 0.3, 0.6, 1) alloys via Kocks and Mecking (KM) plot [42]. The x-axis ($\sigma - \sigma_y$) is scaled by the shear modulus G. The CrCoNi alloy shows the typical multiple-stage hardening, as observed in twinning-induced plasticity (TWIP) alloys. By adding ~13 at.% V, $V_{0.4}Cr_{0.6}CoNi$ first

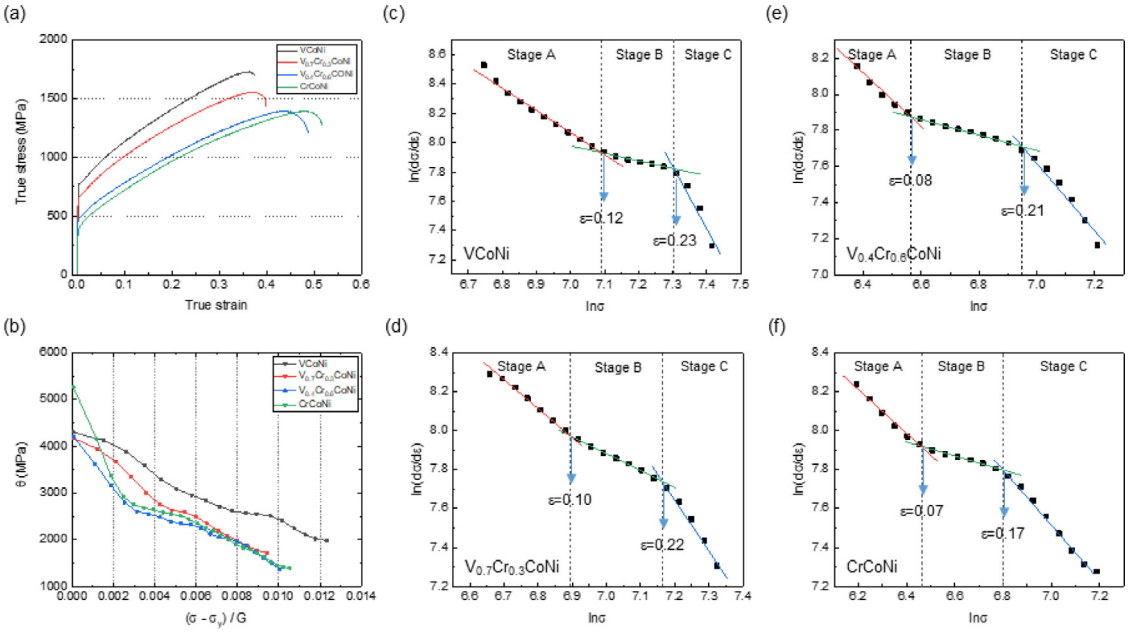

Fig. 5. (a) True stress-strain curve of the VCrCoNi alloys (b) Kocks-Mecking plot of each alloy. Modified Crussard-Jaoul analysis for dividing different deformation stages for the (c) VCoNi, (d) $V_{0.7}Cr_{0.3}CoNi$, (e) $V_{0.4}Cr_{0.6}CoNi$, and (f) CrCoNi alloys.

exhibits a lower hardening rate than CrCoNi until ~2000 MPa, and then overlaps. The hardening rate surpasses that of CrCoNi from $V_{0.7}Cr_{0.3}CoNi$, leading to the highest rate in VCoNi.

To quantitatively investigate the strain-hardening behavior and the transition strains between multiple deformation stages, a modified Crussard-Jaoul analysis based on the Swift equation was carried out as shown in Fig. 5(c–f) [43]. The graphs plot from yield to ultimate tensile strength of true stress-strain curves (Fig. 5(a)). Three stages with different governing deformation mechanisms are observed for each alloy [44–49]. Stage A represents dislocation glides and dynamic recovery, showing a steep decrease with increasing applied tensile strain and stress. Stage *B* shows an activation of secondary deformation mechanism such as deformation twinning or formation of dislocation substructure (interaction of pre-existing and additional slip bands), which leads to a less decrease in hardening rate than that in Stage *A*. Finally, Stage *C* is dominated by dynamic recovery due to an active cross-slip causing more decrease in hardening rate. For each alloy, the transition strains are determined as 0.07, 0.08, 0.10, and 0.12 for stage A,B and 0.17, 0.21, 0.22, and 0.23 for stage B,C. The shift of transition strains between stages is postponed with increasing *V*. In other words, the addition of *V* delays the activation of secondary hardening effect (Stage *B*) and the active dynamic recovery (Stage *C*). Section 4.1 provides a detailed explanation regarding the postponement of transition strains.

3.4. Deformation behaviors at different strains

The aforementioned transitions between stages are closely relevant to the deformation structures. The microstructures in the deformed gage sections near fractured regions after the tensile test were investigated through EBSD. Fig. 6(a_1–d_1) and (a_2–d_2) exhibits IPF maps and image quality (IQ) maps, respectively, for the fully deformed $V_{1-x}Cr_xCoNi$ (x = 0, 0.3, 0.6, 1) alloys. Although the CrCoNi alloy exhibits clear deformation-induced twinning, it is difficult to observe particular secondary deformation structures except for dislocation glides in the *V*-containing alloys.

Figs. 7(a-d) and 8(a-d) present ECCI micrographs showing deformation structures at a sequential tensile strain of 0.05 and 0.2, respectively. At a strain of 0.05 (Fig. 7(a)), the VCoNi alloy shows planar dislocation glides and slip traces well arranged on {111} slip planes. Similar dislocation glide behaviors are found in the $V_{0.7}Cr_{0.3}CoNi$ and $V_{0.4}Cr_{0.6}CoNi$ alloys in Fig. 7(b, c). Dislocations are well aligned on {111} plane also in the CrCoNi alloy (Fig. 7(d)); however, stacking faults are clearly observed, as indicated by white arrows, which are the representative feature found in low-SFE alloys. As the strain increases to 0.2 (Fig. 8(a)), the VCoNi alloy possesses high dislocation density walls (HDDW) along the {111} traces, forming the well-aligned dislocation network substructure, called Taylor lattice. The $V_{0.7}Cr_{0.3}CoNi$ and $V_{0.4}Cr_{0.6}CoNi$ alloys in Fig. 8(b, c) exhibit similar dislocation substructures to the VCoNi alloy with no onset of any other deformation mechanisms. In the CrCoNi alloy, however, the deformation-induced twinning is clearly observed with a clear contrast difference (Fig. 8(d)), which well corresponds to the EBSD observation (Fig. 6(d_1, d_2)). The nanotwins possess a width and mean spacing of ~50 nm and ~200 nm, respectively.

4. Discussion

4.1. Planar slip behavior in V-containing $V_{1-x}Cr_xCoNi$ alloys

The slip behaviors and deformation mechanisms of each $V_{1-x}Cr_xCoNi$ (x = 0, 0.3, 0.6, 1) alloy were investigated at sequential strains, as described in Section 3.4. The CrCoNi alloy shows stacking faults in the early stage of deformation, indicated by white arrows in Fig. 7(d), which were further developed into deformation-induced nanotwins as the strain increases (Fig. 8(d)). Meanwhile, the VCoNi alloy only exhibits planar slip behavior over the entire deformation ranges, forming dislocation network substructures. Of particular interest is the suppression of SFs and twins in the $V_{0.4}Cr_{0.6}CoNi$ alloy indicating the slip behavior is altered by a small addition of 13 at.% V to the CrCoNi alloy. Therefore, *V* is expected to play a critical role in determining the deformation mechanism.

To confirm the effect of *V* on deformation mechanism, we conducted *ab initio* SFE calculations for the $V_{1-x}Cr_xCoNi$ alloys. From Fig. 9, at 300 K a small addition (13 at.%) of V content is found to sensitively increase the SFE by ≈20 mJ m^{-2} from the SFE of Cr-

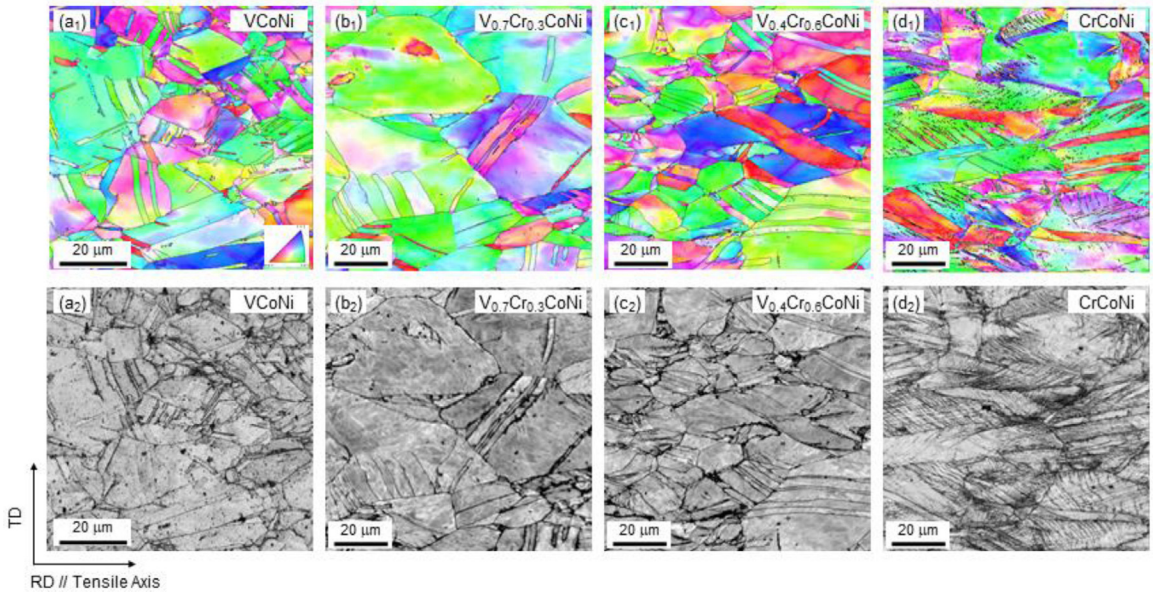

Fig. 6. EBSD IPF and IQ maps for the fully deformed VCrCoNi alloys with similar grain sizes.

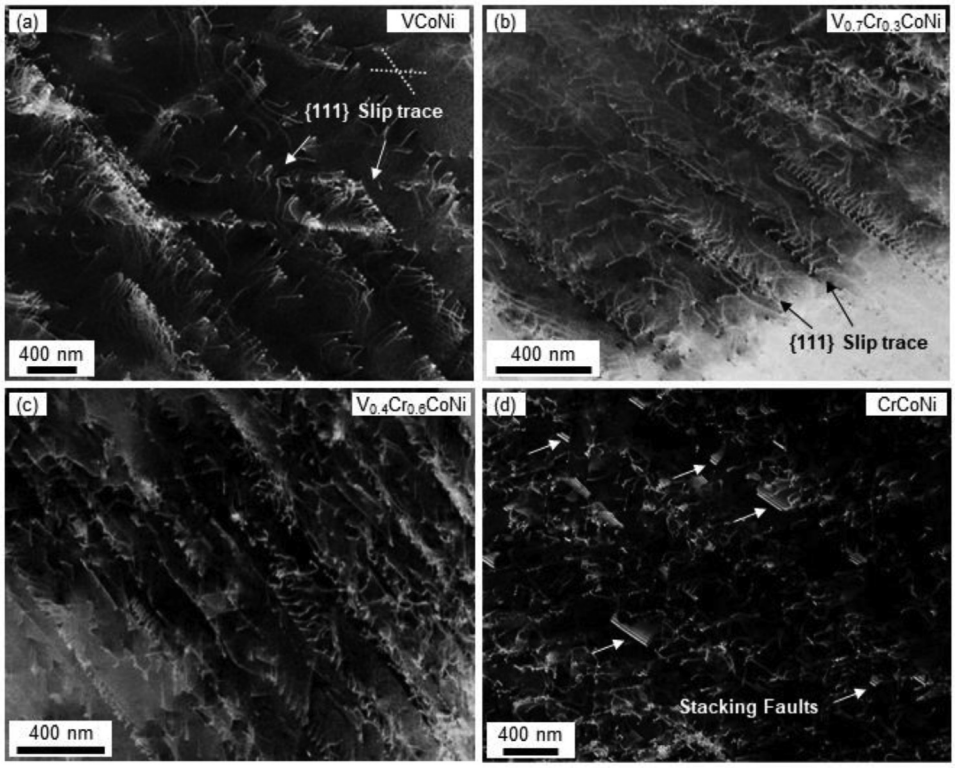

Fig. 7. ECCI micrographs of deformation structures at the strain of 0.05 for (a) VCoNi, (b) $V_{0.7}Cr_{0.3}CoNi$, (c) $V_{0.4}Cr_{0.6}CoNi$, and (d) CrCoNi alloys. White arrows indicate stacking faults (SF).

CoNi. More *V* (23 at.%) further increases the SFE by ≈50 mJ m^{-2} from the SFE of CrCoNi, while further V addition does not show a substantial SFE increase anymore. Note that these calculations at 300 K were carried out considering lattice vibrations [50–52] but without taking other excitations into account. From Fig. 9, lattice vibrations are found to substantially increase the SFE of CrCoNi, while the impact on the SFE of *V*-rich $V_{1-x}Cr_xCoNi$ is marginal. The ≈10 mJ m^{-2} SFE increase of CrCoNi at 300 K is in good agreement with previous *ab initio* calculations [51]. Nevertheless, the obtained SFE of CrCoNi at 300 K is −20 mJ m^{-2}, which is still lower than an experimentally measured SFE of 22 ± 4 mJ m^{-2} [5]. Other finite-temperature excitations such as magnetic fluctuations [50,53,54], not considered in the present calculations, may reduce this discrepancy. Consideration of chemical SRO in CrCoNi may also increase the SFE of CrCoNi [13,55]. However, despite such absolute shifts of computed SFEs, compositional trends from *ab initio* are typically rather robust. To give an example, for the Cantor alloy, for instance, the SFE can be larger if calculations are performed at the experimental lattice constants (being significantly larger as computationally predicted) whereas chemical trends are hardly af-

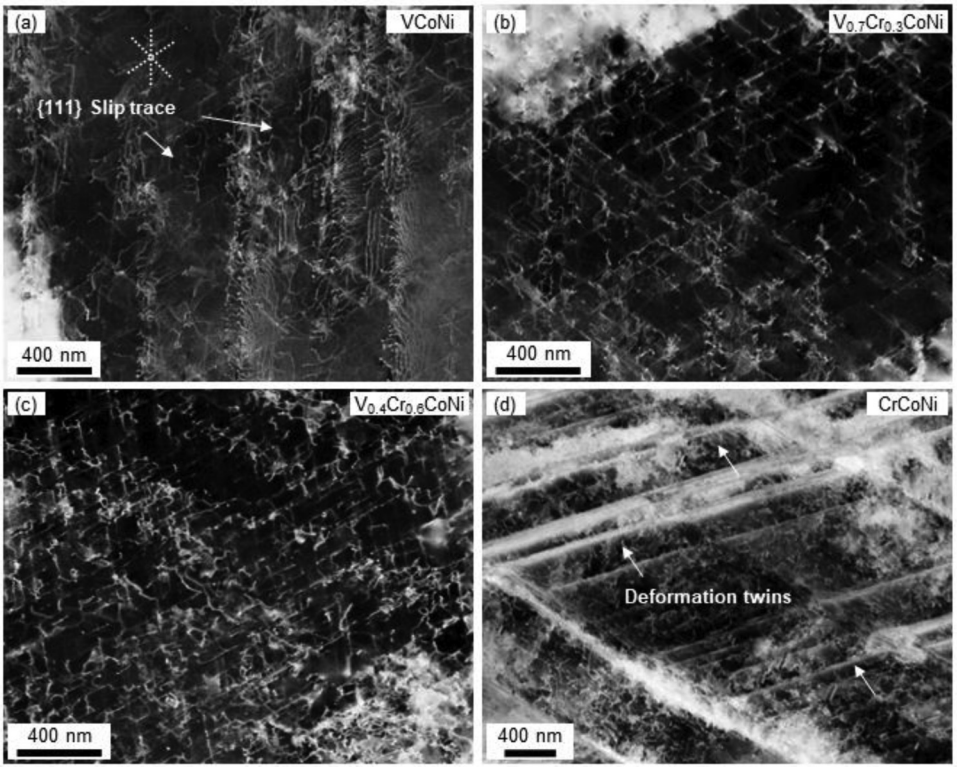

Fig. 8. ECCI micrographs of deformation structures at the strain of 0.2 for (a) VCoNi with white dashed line of {111} slip trace, (b) $V_{0.7}Cr_{0.3}CoNi$, (c) $V_{0.4}Cr_{0.6}CoNi$, and (d) CrCoNi alloys. White arrows indicate deformation twins.

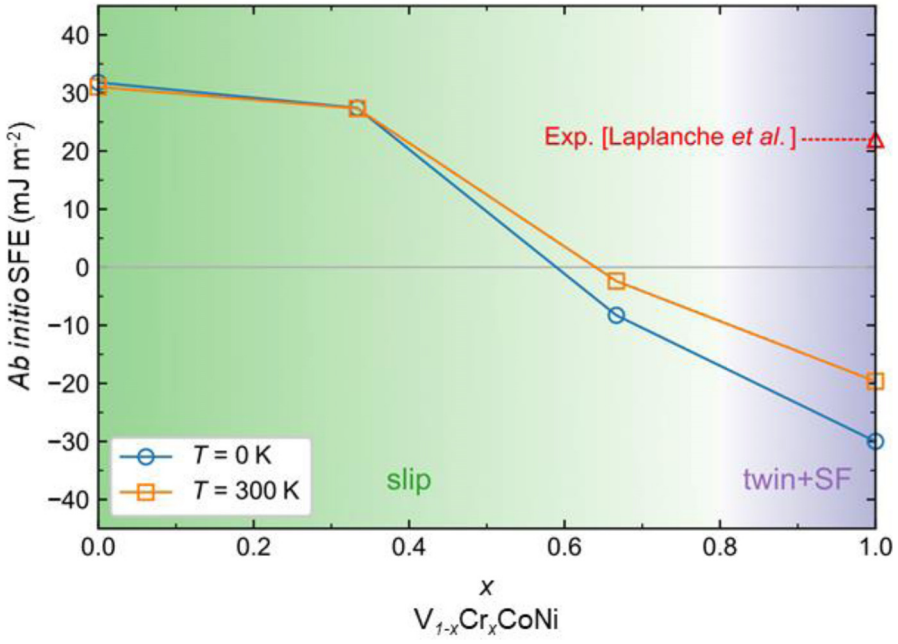

Fig. 9. *Ab initio* computed SFEs at the fcc lattice parameter of 3.6 Å. Blue circles represent the results at 0 K, and orange squares represent the results at 300 K with lattice vibrational contributions. The red triangle demonstrates an experimental SFE of CrCoNi [5].

fected [50]. We therefore focus in the present study on the variation of the SFEs due to the compositional variation and discuss it in relation with the experimental observation.

Generally in fcc-structured metals and alloys, SFE is a useful parameter for determining the deformation mechanism. Increasing SFE is known to hinder the formation of SFs and subsequent nucleation of twins and also enhance the activity of cross-slip and dynamic recovery. Although the border is not absolute, alloys with very low SFEs (<20 mJ m^{-2}) show typically deformation-induced martensitic transformation and those with medium SFEs (20–50 mJ m^{-2}) exhibit deformation-induced twinning. These classifications well predict the deformation mechanism in transformation-induced plasticity (TRIP) and TWIP steels such as austenitic stainless steels, high-Mn steels, and lightweight steels

[49,56–59]. As well as the mentioned austenitic steels, for the alloys dominantly exhibiting dislocation-mediated plasticity, such as Al and Cu alloys, the SFE varies from 210 mJ m^{-2} to 7 mJ m^{-2} and from 80 mJ m^{-2} to 4 mJ m^{-2}, respectively. The dislocation configuration of the alloys changes from cell (wavy) to Taylor lattices (coplanar) at SFE value of ~20 mJ m^{-2} [60,61].

The planar slip behavior generally originates from a low SFE, where a perfect dislocation splits into two broad Shockley partial dislocations therefore making it hard to cross-slip, but it is also observed in alloys with high SFE [44]. In other words, the SFE is not a rigid parameter determining the deformation mechanism. Instead, SRO has been suggested as a crucial parameter to cause the planar slip behavior in those alloys owing to the glide plane softening effect [17,44]. The SRO acts as an obstacle for dislocation glide and enables the first dislocation to require a higher stress. Then, the next dislocations follow the first one from the activated dislocation source, which assist to overcome the high resistance. After the destruction of the SRO by the first dislocation, the accelerated slip localizes the gliding to a single slip plane. Recent studies have reported the existence of SRO in CrCoNi alloy by employing a DFT-based Monte Carlo approach and also experimentally using energy-filtered transmission electron microscopy [62,63]. They revealed the impact of SRO on SFE by comparing the separation of partial dislocation pairs between water-quenched and aged specimens. Although SRO in the aged specimen induces a more compact separation of the dislocation pairs, it shows a planar slip behavior. In this study, all the specimens were water-quenched after isothermal heat treatments; thus, there might be insufficient time for constructing effective SROs for SFE [62]. Regarding the existence of SRO in VCoNi, Kostiuchenko et al. reported that the presence of SRO affects very little to the overall lattice distortions [15]. On the other hand, Chen et al. [64] recently observed chemical short-range order (CSRO) in the VCoNi alloy which led to profuse dislocation tangles rather than planar slip. In the current VCoNi alloy fabricated by relatively different heat treatment conditions, however, the planar slip is rather the main deformation mechanism, the SRO or CSRO seems not to play a dominant role. The CSRO would also depend on the content of Cr and *V*, thus further systematic investigations are required to unravel its role on the deformation behaviors. Hence, speculating another factor rather than the SFE or SRO for the planar slip, we shed light on the large solid-solution strengthening effect as a key parameter.

As mentioned above, planar slip occurs due to slip localizations in the absence of cross-slip. In this regard, investigating the cause for hindering cross-slip is of interest. For a dislocation to cross-slip based on the Friedel-Escaig mechanism [65], the dissociated partials must join as perfect dislocation, i.e., the dissociated partials must overcome the friction stress to combine. Hong and Laird [66] reported the required force for joining partials in terms of SFE and frictional force which is imposed by solute atoms. The relevant equations can be simply written as follows:

$$F_t = \gamma - F_r - a F_f \tag{3}$$

where F_t is the total force required to join the partials, γ is the SFE, F_r is the repulsive force between two partials, α is the number of partials (=2), and F_f is the frictional force imposed by solute atoms. As the term F_r is independent from the alloying effect [66], the order of F_t is determined by a balance between the former SFE and the latter frictional term. To further understand Eq. (3), the authors implied when the reciprocal width (W_R) is enough to reach the critical value, i.e., the W_R is smaller than the critical value, the slip mode alters from wavy to planar at room temperature. The reciprocal width can be calculated as follows:

$$W_R = \gamma / G - 2(1+\nu)\, b_e\, \Omega C / \pi (1-\nu) \tag{4}$$

where G is the shear modulus, ν is the Poisson's ratio, b_e is the edge component of Burger's vector, Ω is the atomic size misfit parameter, and C is the atomic solute content. On the right-hand side of Eq. (4), the first term indicates the SFE term, and the second term explains the frictional force term imposed by the solute atoms. The latter frictional force term is dominantly affected by the atomic size misfit parameter and solute content.

Hence, the slip behavior of the alloy can be determined by the frictional force term when the frictional force becomes more dominant than the SFE. According to the correlation between the SD of the atomic-level pressure and solid-solution strength (Fig. 3), the increasing deviation induces higher solid-solution strengthening and the higher strength which pins points for dislocation motion. Recently Lee et al. [67,68] reported by molecular dynamics simulations that high-strength pinning points affect the critical force required for dislocation glide initiation. Therefore, it is reasonable to suppose that the addition of *V* induces higher friction stress to partial dislocations, thus retarding cross-slip than CrCoNi alloy in the absence of *V*.

For the $V_{1-x}Cr_xCoNi$ alloys, a large increase in the friction stress (solid-solution strength) is expected to overrate the increase in SFE owing to the addition of *V* to CrCoNi. Therefore, the partial dislocations are inhibited to join one another, leading to planar glide due to low cross-slip activity. Furthermore, the suppression of cross-slip retards the dislocation rearrangement rate, which results in the higher strain hardening rate. The combination of high SFE and high solid-solution strength leads to the absence of secondary deformation mechanism and planar slip behavior for the *V*-containing $V_{1-x}Cr_xCoNi$ (x = 0, 0.3, 0.6) alloys. Although the deformation mechanisms of the current alloys have been discussed so far, the genuine question still remains unsolved regarding the higher strain-hardening rate in planar slip behavior in *V*-rich $V_{1-x}Cr_xCoNi$ (x = 0, 0.3) alloys than the rate in TWIP of CrCoNi alloy.

4.2. Strain-hardening rate in V-containing $V_{1-x}Cr_xCoNi$ alloys

Generally, alloys showing TRIP or TWIP display a higher strain-hardening rate than those deforming predominantly by dislocation-mediated plasticity. These secondary deformation mechanisms introduce additional barriers for dislocation movements such as martensite platelets and twin boundaries, via the dynamic Hall-Petch effect. Nonetheless, it is noteworthy to mention that the strain-hardening rate by the only dislocation-mediated plasticity can outstrip the rate by deformation-induced twinning hardening for the alloys with high solid-solution strength such in *V*-rich $V_{1-x}Cr_xCoNi$ (x = 0, 0.3) alloys.

As discussed above, owing to the high solid-solution strength with the addition of *V*, planar-slip behavior leads to the formation of HDDW. These HDDWs that possess long-range stress fields build nanosized dislocation substructures, i.e., dynamic slip band refinement [69]. The generation of these dislocation substructures causes massive pinning of dislocations and a satisfactory strain-hardening effect even without any secondary deformation mechanism [8,70]. The delay in the activation of dynamic recovery enables the maintenance of a high initial strain-hardening rate, resulting in a high overall strain-hardening rate. Comparing the TWIP with the slip, the dynamic Hall-Petch effect in CrCoNi is superior for strain hardening to the slip band refinement in $V_{0.4}Cr_{0.6}CoNi$. However, as the V content increases further in $V_{0.7}Cr_{0.3}CoNi$ and VCoNi, the dislocation-mediated plasticity of high solid-solution strength alloys can induce the higher strain-hardening rate than that of the TWIP CrCoNi alloy.

To reveal the underlying mechanism for the higher hardening rate in $V_{0.7}Cr_{0.3}CoNi$ and VCoNi alloys, an approach of the Kocks-Mecking model has been conducted. According to this model, the

strain-hardening rate can be expressed as follows according to the Kocks and Mecking model [42]:

$$\theta = \theta_0 - \theta_r(T, \dot{\gamma}) \quad (5)$$

where θ is the total work hardening rate, and θ_0 and θ_r represent the constant hardening (athermal), and dynamic recovery terms, respectively. The athermal term (θ_0) is inversely proportional to the dislocation mean free path [42,71]. The dynamic recovery is determined through complicated interactions between the local stress and the local strength at the recovery sites; dislocation interacting sites. For recovery to occur in the recovery sites, sufficient applied stresses or aids of thermal activation are required. Kocks and Mecking [42] introduced the stress-dependent activation energy as the Gibbs free energy as follows:

$\Delta G = \Delta G([\tau + \tau_F])/\tau_M)$ (6) where τ is the applied flow stress, τ_F is the local forward stress as the "dipole pile-up" stress, and τ_M is the local resistance strength as the obstacle-dislocation density. The high solid-solution strength increases the local resistance strength and thus retards the recovery rate as discussed in Section 4.1. Considering the KM plot in Fig. 5(b) isolating the contribution from dislocation multiplication, the observed slope at the early strain levels (Stage *A*) becomes gradual with increasing *V*. The change in slope well supports the effect of the solid-solution strength on the strain-hardening rate in terms of the recovery rate.

Further investigating the strain hardening behaviors quantitatively, the Crussard-Jaoul analysis was carried out as in Fig. 5(c–f). Typical multi-stages of the TWIP alloys of fine grains were observed for the CrCoNi alloy. In Stage *A* until a strain of 0.07, only dislocation glide and dynamic recovery exist with no formation of mechanical twinning. Nano-twinning occurs as the main work hardening deformation mechanism in Stage *B* between 0.07 and 0.17 providing extra boundaries to dislocation glide. Finally in Stage *C*, thicker bundles are formed and the high-rate dynamic recovery takes place. On the other hand, the other three alloys ($V_{1-x}Cr_xCoNi$ (x = 0, 0.3, 0.6)) similarly show three stages like the CrCoNi alloy but very different strain hardening behaviors as observed in Figs. 6–8. Regardless of the high SFE, slip bands are formed by planar slip behavior due to high solid-solution strength in Stage *A*. The activation of additional non-coplanar slip systems leads to slip band refinement effect by mutual intersections of slip bands in Stage *B*. Note that transition in Stage *A* and Stage *B* is delayed as the *V* content increases. The delay of activation of additional non-coplanar slip systems is expected from the difficult generation of dislocation source with increasing *V* and the obstruction of cross-slip [69]. Similarly, the transition from Stage *B* to Stage *C* is observed to be delayed as well with increasing *V*, which is related to the active cross-slip and prevalent dynamic recovery.

Therefore, impeding the cross-slip activation due to high solid-solution strength is expected to be the explanation for the delayed transition strains with increasing *V*. Reminding the fact that the lower cross-slip activity decreases the dislocation rearrangement rate, which in turn increases the strain-hardening rate, thus the higher work hardening rate of *V*-rich alloys than *V*-depleted alloys can be clarified. Therefore, the overall higher strain hardening rate of *V*-rich alloys can be explained by delaying the decrease in hardening rate with active retardation of cross-slip by high solid-solution strength.

5. Conclusion

In this study, the degree of the solid-solution strengthening effect was controlled by fabricating medium-entropy $V_{1-x}Cr_xCoNi$ (x = 0, 0.3, 0.6, 1) alloys and its effect on deformation mechanisms and strain hardening was investigated. The strain-hardening rate obtained for the dislocation-mediated plasticity was higher than the rate of TWIP under the activated huge solid-solution strengthening effect. The underlying mechanisms were discussed in terms of elemental effects, solid-solution strengthening, atomic-level pressure, SFEs, and transitions of deformation mechanisms, thus leading to the following conclusions:

(1) The solid-solution strength (σ_0), defined by the Hall-Petch relation, increased from CrCoNi to VCoNi with the addition of *V*. The calculated difference in atomic size misfit and electronegativity, MSAD, SD of Bader charge (charge transfer), and atomic-level pressure indicated a linearly increasing relationship with the experimentally measured solid-solution strength.
(2) The Hall-Petch coefficient (k_y) was also enhanced with increasing *V* content. Moreover, the overall relationship between σ_0 and k_y was almost linearly proportional from pure metals to HEAs and MEAs. This relationship indicates that an increase in solid-solution strength has a strong tendency with an increase in grain-size sensitivity to strengthening.
(3) The CrCoNi alloy, which is a known alloy with a low SFE, showed deformation-induced twinning. However, the other alloys containing *V* only exhibited dislocation glides, specifically planar slip and consequent nanosized dislocation substructures, despite high SFEs. The slip behavior could be determined by the frictional force term under the predominant frictional force compared to the SFE. The addition of *V* induced higher friction stress to partial dislocations thus retarding cross-slip than CrCoNi alloy.
(4) Comparing the TWIP of CrCoNi with the slip of $V_{0.4}Cr_{0.6}CoNi$, the dynamic Hall-Petch effect in CrCoNi was superior for strain hardening to the slip band refinement in $V_{0.4}Cr_{0.6}CoNi$. However, as *V* content increased further to $V_{0.7}Cr_{0.3}CoNi$ and VCoNi, the slip in $V_{0.7}Cr_{0.3}CoNi$ and VCoNi with high solid-solution strength surpassed the rate of CrCoNi.
(5) The shift in transition strains between multiple deformation stages was postponed with increasing *V* in the modified Crussard-Jaoul analysis. The lowered cross-slip activation due to the high solid-solution strength retarded the dislocation rearrangement rate, i.e., dynamic recovery, thus increasing the strain hardening rate. Therefore, the overall higher strain-hardening rate of *V*-rich alloys can be attributed to the delay of hardening-rate decrease with active retardation of cross-slip by high solid-solution strength.

Declaration of Competing Interest

The authors declare that they have no known competing financial interests or personal relationships that could have appeared to influence the work reported in this paper.

Acknowledgments

This work was financially supported by the POSCO Science Fellowship of POSCO TJ Park Foundation, the National Research Foundation of Korea (No. NRF-2020R1C1C1003554), the Creative Materials Discovery Program of the National Research Foundation of Korea (NRF) funded by the Ministry of Science and ICT (No. NRF-2016M3D1A1023384) and the Korea Institute for Advancement of Technology (KIAT) grant funded by the Korea Government (MOTIE, P0002019, The Competency Development Program for Industry Specialist). F.K. gratefully acknowledges support from the German Research Foundation (Deutsche Forschungsgemeinschaft, DFG) under the priority program 2006 "CCA – HEA". We thank Andrei V. Ruban for providing the code to generate SQSs.

Supplementary materials

Supplementary material associated with this article can be found, in the online version, at doi:10.1016/j.jmst.2021.07.042.

References

[1] B. Cantor, I.T.H. Chang, P. Knight, A.J.B. Vincent, Mater. Sci. Eng. A 375–377 (2004) 213–218.
[2] J.W. Yeh, S.K. Chen, S.J. Lin, J.Y. Gan, T.S. Chin, T.T. Shun, C.H. Tsau, S.Y. Chang, Adv. Eng. Mater. 6 (2004) 299–303.
[3] Y.A. Alshataif, S. Sivasankaran, F.A. Al-Mufadi, A.S. Alaboodi, H.R. Ammar, Met. Mater. Int. 26 (2020) 1099–1133.
[4] B. Gludovatz, A. Hohenwarter, K.V.S. Thurston, H. Bei, Z. Wu, E.P. George, R.O. Ritchie, Nat. Commun. 7 (2016) 1–8.
[5] G. Laplanche, A. Kostka, C. Reinhart, J. Hunfeld, G. Eggeler, E.P. George, Acta Mater. 128 (2017) 292–303.
[6] Y. Chen, X. An, Z. Zhou, P. Munroe, S. Zhang, X. Liao, Z. Xie, Sci. China Mater. 64 (2021) 209–222.
[7] J. Miao, C.E. Slone, T.M. Smith, C. Niu, H. Bei, M. Ghazisaeidi, G.M. Pharr, M.J. Mills, Acta Mater. 132 (2017) 35–48.
[8] S.S. Sohn, A. Kwiatkowski da Silva, Y. Ikeda, F. Körmann, W. Lu, W.S. Choi, B. Gault, D. Ponge, J. Neugebauer, D. Raabe, Adv. Mater. 31 (2019) 1–8.
[9] D.C. Yang, Y.H. Jo, Y. Ikeda, F. Körmann, S.S. Sohn, J. Mater. Sci. Technol. 90 (2021) 159–167.
[10] B. Yin, F. Maresca, W.A. Curtin, Acta Mater. 188 (2020) 486–491.
[11] H.S. Oh, S.J. Kim, K. Odbadrakh, W.H. Ryu, K.N. Yoon, S. Mu, F. Körmann, Y. Ikeda, C.C. Tasan, D. Raabe, T. Egami, E.S. Park, Nat. Commun. 10 (2019) 1–8.
[12] S. Yoshida, T. Ikeuchi, T. Bhattacharjee, Y. Bai, A. Shibata, N. Tsuji, Acta Mater. 171 (2019) 201–215.
[13] J. Ding, Q. Yu, M. Asta, R.O. Ritchie, Proc. Natl. Acad. Sci. U. S. A. 115 (2018) 8919–8924.
[14] S.S. Sohn, D.G. Kim, Y.H. Jo, A.K. da Silva, W. Lu, A.J. Breen, B. Gault, D. Ponge, Acta Mater. 194 (2020) 106–117.
[15] T. Kostiuchenko, A.V. Ruban, J. Neugebauer, A. Shapeev, F. Körmann, Phys. Rev. Mater. 4 (2020) 1–11.
[16] D.A. Hughes, Acta Metall. Mater. 41 (1993) 1421–1430.
[17] V. Gerold, H.P. Karnthaler, Acta Metall. 37 (1989) 2177–2183.
[18] J.P. McINTYRE, W.H. Scotland, Glasg. Med. J. 32 (1951) 268–721951.
[19] A. Zunger, S.H. Wei, L.G. Ferreira, J.E. Bernard, Phys. Rev. Lett. 65 (1990) 353–356.
[20] G. Kresse, J. Non Cryst. Solids 192–193 (1995) 222–229.
[21] G. Kresse, J. Furthmüller, Comput. Mater. Sci. 6 (1996) 15–50.
[22] D. Joubert, Phys. Rev. B 59 (1999) 1758–1775.
[23] P.E. Blöchl, Phys. Rev. B 50 (1994) 17953–17979.
[24] J.P. Perdew, K. Burke, M. Ernzerhof, Phys. Rev. Lett. 77 (1996) 3865–3868.
[25] M. Methfessel, A.T. Paxton, Phys. Rev. B 40 (1989) 3616–3621.
[26] A. Otero-De-La-Roza, D. Abbasi-Pérez, V. Luaña, Comput. Phys. Commun. 182 (2011) 2232–2248.
[27] A. Otero-De-La-Roza, V. Luaña, Comput. Phys. Commun. 182 (2011) 1708–1720.
[28] P. Vinet, J.R. Smith, J. Ferrante, J.H. Rose, Phys. Rev. B 35 (1987) 1945–1953.
[29] P.J.H. Denteneer, W. Van Haeringen, J. Phys. C Solid State Phys. 20 (1987) L883–L887.
[30] G. Henkelman, A. Arnaldsson, H. Jónsson, Comput. Mater. Sci. 36 (2006) 354–360.
[31] S. Ishibashi, T. Tamura, S. Tanaka, M. Kohyama, K. Terakura, Phys. Rev. B 76 (2007) 3–6.
[32] C.L. Fu, K.M. Ho, Phys. Rev. B 28 (1983) 5480–5486.
[33] A. Filippetti, V. Fiorentini, Phys. Rev. B 61 (2000) 8433–8442.
[34] Y. Shiihara, M. Kohyama, S. Ishibashi, Phys. Rev. B 81 (2010) 1–11.
[35] Y. Zhang, Y.J. Zhou, J.P. Lin, G.L. Chen, P.K. Liaw, Adv. Eng. Mater. 10 (2008) 534–538.
[36] X. Yang, Y. Zhang, Mater. Chem. Phys. 132 (2012) 233–238.
[37] R. Labusch, Phys. Status Solidi 41 (1970) 659–669.
[38] N.L. Okamoto, K. Yuge, K. Tanaka, H. Inui, E.P. George, AIP Adv. 6 (2016) 125008.
[39] C.X. Ren, Q. Wang, J.P. Hou, Z.J. Zhang, H.J. Yang, Z.F. Zhang, Mater. Sci. Eng. A 786 (2020) 139441.
[40] M. Schneider, E.P. George, T.J. Manescau, T. Záležák, J. Hunfeld, A. Dlouhý, G. Eggeler, G. Laplanche, Int. J. Plast. 124 (2020) 155–169.
[41] G.W. Hu, L.C. Zeng, H. Du, X.W. Liu, Y. Wu, P. Gong, Z.T. Fan, Q. Hu, E.P. George, J. Mater. Sci. Technol. 54 (2020) 196–205.
[42] U.F. Kocks, H. Mecking, Prog. Mater. Sci. 48 (2003) 171–273.
[43] B.K. Jha, R. Avtar, V.S. Dwivedi, V. Ramaswamy, J. Mater. Sci. Lett. 6 (1987) 891–893.
[44] E. Welsch, D. Ponge, S.M. Hafez Haghighat, S. Sandlöbes, P. Choi, M. Herbig, S. Zaefferer, D. Raabe, Acta Mater. 116 (2016) 188–199.
[45] S. Asgari, E. El-Danaf, S.R. Kalidindi, R.D. Doherty, Metall. Mater. Trans. A 28 (1997) 1781–1795.
[46] L. Zhao, D. Zhu, L. Liu, Z. Hu, M. Wang, Acta Metall. Sin. (Engl. Lett.) 27 (2014) 601–608.
[47] J.E. Jin, Y.K. Lee, Mater. Sci. Eng. A 527 (2009) 157–161.
[48] G.C. Soares, M.C.M. Rodrigues, L. De Arruda Santos, Mater. Res. 20 (2017) 141–151 http://dx.doi.org/10.1590/1980-5373-MR-2016-0932.
[49] I. Gutierrez-Urrutia, D. Raabe, Acta Mater. 59 (2011) 6449–6462.
[50] Z. Li, F. Körmann, B. Grabowski, J. Neugebauer, D. Raabe, Acta Mater. 136 (2017) 262–270.
[51] S. Zhao, G.M. Stocks, Y. Zhang, Acta Mater. 134 (2017) 334–345.
[52] C. Niu, C.R. LaRosa, J. Miao, M.J. Mills, M. Ghazisaeidi, Nat. Commun. 9 (2018) 1–9.
[53] S. Huang, W. Li, S. Lu, F. Tian, J. Shen, E. Holmström, L. Vitos, Scr. Mater. 108 (2015) 44–47.
[54] Z. Dong, S. Schönecker, W. Li, D. Chen, L. Vitos, Sci. Rep. 8 (2018) 4–10.
[55] Y. Ikeda, F. Körmann, I. Tanaka, J. Neugebauer, Entropy 20 (2018) 655.
[56] K. Jeong, J.E. Jin, Y.S. Jung, S. Kang, Y.K. Lee, Acta Mater. 61 (2013) 3399–3410.
[57] B.C. De Cooman, Y. Estrin, S.K. Kim, Acta Mater. 142 (2018) 283–362.
[58] D.T. Pierce, J.A. Jiménez, J. Bentley, D. Raabe, J.E. Wittig, Acta Mater. 100 (2015) 178–190.
[59] N. Saeidi, M. Jafari, J.G. Kim, F. Ashrafizadeh, H.S. Kim, Met. Mater. Int. 26 (2020) 168–178.
[60] A. Dhal, S.K. Panigrahi, M.S. Shunmugam, J. Alloys Compd. 726 (2017) 1205–1219.
[61] A. Rohatgi, K.S. Vecchio, G.T. Gray, Metall. Mater. Trans. A 32 (2001) 135–145.
[62] R. Zhang, S. Zhao, J. Ding, Y. Chong, T. Jia, C. Ophus, M. Asta, R.O. Ritchie, A.M. Minor, Nature 581 (2020) 283–287.
[63] A. Tamm, A. Aabloo, M. Klintenberg, M. Stocks, A. Caro, Acta Mater. 99 (2015) 307–312.
[64] X. Chen, Q. Wang, Z. Cheng, M. Zhu, H. Zhou, P. Jiang, L. Zhou, Q. Xue, F. Yuan, J. Zhu, X. Wu, E. Ma, Nature 592 (2021) 712–716.
[65] J. Bonneville, B. Escaig, Acta Metall. 27 (1979) 1477–1486.
[66] S.I. Hong, C. Laird, Acta Metall. Mater. 38 (1990) 1581–1594.
[67] S. Lee, M.J. Duarte, M. Feuerbacher, R. Soler, C. Kirchlechner, C.H. Liebscher, S.H. Oh, G. Dehm, Mater. Res. Lett. 8 (2020) 216–224.
[68] D. Utt, S. Lee, A. Stukowski, S.H. Oh, G. Dehm, K. Albe, ArXiv (2020) 2007.11489 https://arxiv.org/abs/2007.
[69] E. Welsch, D. Ponge, S.M. Hafez Haghighat, S. Sandlöbes, P. Choi, M. Herbig, S. Zaefferer, D. Raabe, Acta Mater. 116 (2016) 188–199.
[70] R. Xiong, Y. Liu, H. Si, H. Peng, S. Wang, B. Sun, H. Chen, H.S. Kim, Y. Wen, Met. Mater. Int. 27 (2021) 3891–3904.
[71] L. Kubin, B. Devincre, T. Hoc, Acta Mater. 56 (2008) 6040–6049.
[72] S. Ishibashi, Y. Ikeda, F. Körmann, B. Grabowski, J. Neugebauer, Phys. Rev. Mater. 4 (2020) 023608.